High-Fidelity Aeropropulsive Optimization of a Mail-Slot Distributed Electric Propulsion System for the SUSAN Electrofan

Joshua L. Anibal and Jared C. Duensing
NASA Ames Research Center, Mountain View, California

Hybrid- and all-electric aircraft concepts use electric motors for power rather than a conventional jet engine. Electric propulsors open the door to new ways to synergistically integrate the propulsion system with the airframe. For example, many small electric propulsors can be distributed along the wing to increase the effective bypass ratio for better overall efficiency. Furthermore, these propulsors can be attached to the wing surface for boundary layer ingestion (BLI) to further the efficiency gains. However, these novel methods of aeropropulsive integration also create challenges such as nonuniform inflow and complex nacelle geometries. Here we use gradient-based aerodynamic shape optimization to address the design challenges of the wing-mounted distributed electric propulsion system of the Subsonic Single Aft Engine (SUSAN) concept. In doing so, we aim to more accurately benchmark the flow power of SUSAN's mailslot propulsors relative to a conventional propulsion system in both an isolated and BLI configuration. Our preliminary results found that relative to an optimized podded propulsor the optimized mailslot and BLI mailslot designs required 9% and 15% more power respectively. We found that this increase in power was needed to offset the increased drag of the mailslot and boundary layer ingestion (BLI) mailslot propulsors.

I. Introduction

Hybrid-electric aircraft offer a means to reduce the carbon footprint of aviation [1]. However, there remain uncertainties about hybrid-electric technologies and the design of aircraft that use them. NASA has been investigating hybrid-electric technology through the development of the Subsonic Single Aft Engine (SUSAN) Electrofan concept [2]. The SUSAN aircraft uses turboelectric hybridization, meaning a portion of the shaft power produced by a jet fuel burning engine is converted to electricity to power additional electric propulsors. The scale-independent nature of electric propulsors allows aircraft designers to integrate them into the airframe in novel ways to produce additional aeropropulsive benefits. For example, the propulsors could be positioned to ingest the boundary layer of the wing or placed so their exhaust helps keep the flow attached at high angles of attack. In the case of SUSAN, the propulsors are positioned under the wing near the trailing edge to ingest the boundary layer. Furthermore, the propulsors are connected span-wise to reduce the total wetted area and share an external surface to avoid shocks between adjacent nacelles. This arrangement is called a mailslot configuration [3]. This novel concept for propulsion airframe integration (PAI) is highlighted in blue in Fig. 1.

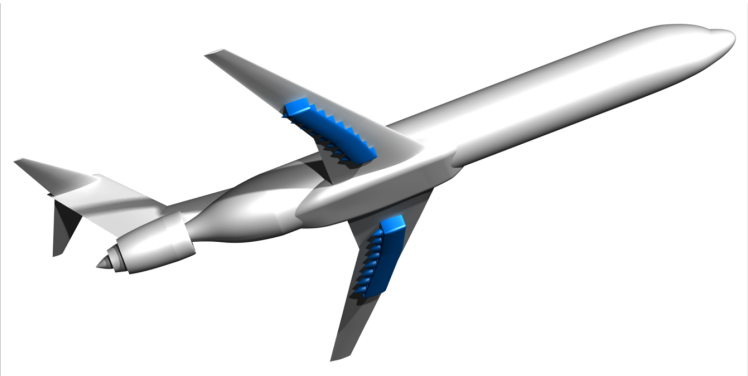


Fig. 1 The SUSAN concept shown with the mailslot propulsors highlighted in blue.

However, integrating the propulsors into the wing in novel ways also produces new challenges. For a wing mounted BLI propulsor for example, the air at the inlet may need to be diffused more to meet the same fan face Mach number requirement as a free-flying propulsor. Although the air inside the boundary layer of the wing is slowed, the air outside the boundary layer is typically accelerated as it moves around the airfoil. For transonic distributed electric propulsion (DEP) designs, the sweep of the wings causes a corresponding offset in the propulsors that span the wing. This offset creates asymmetric conditions at the inlet and outlet of the propulsors. Additionally, the design of a mailslot propulsor introduces additional geometric challenges. This arrangement requires the geometry of the propulsors to be repeatable in the span-wise-direction. To avoid gaps between adjacent propulsors the inlet and outlet of the propulsor must be the widest part of the nacelle duct.

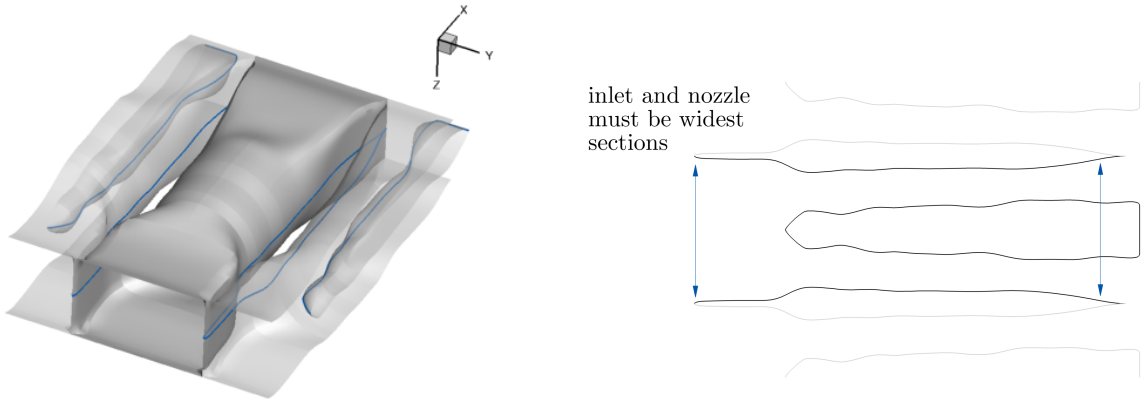


Fig. 2 The geometry of the duct must be widest at the inlet and the nozzle so that it can be repeated to form a continuous mailslot without gaps.

Generally, computational fluid dynamics (CFD) analysis is useful for resolving the flow features of a novel propulsion integration concept like the mailslot. Previous authors have used CFD to iterate on the design of propulsors integrated into the wing. Wick et al. [4] performed a vast parametric study of DEP concepts using 3-dimensional Reynolds-averaged Navier–Stokes (RANS) CFD. Schmollgruber et al. [5] also used CFD to explore the design of an array of BLI ingesting mounted fans with RANS CFD for the DRAGON concept aircraft. When assessing the performance of a single propulsor embedded in a wing with RANS CFD, Lee and Liou [6] found a shaft power savings ranging from 13-23%.

Machado et al. [7] performed optimization of SUSAN's tail cone thruster and iterated the design of SUSAN's mailslot propulsors by hand. The design of the mailslot propulsors has proved challenging, yet estimates indicate that it offers potential fuel savings over a conventional design [3, 8]. However, the mailslot in this past work [3, 8] has been idealized by applying the thrust of the fan over rectangular cross-sections of the duct.

Other authors used CFD in conjunction with numerical optimization to refine the design of propulsors. To study the effects of pressure ratio Yildirim et al. [9] introduced a fully coupled cycle analysis model with either an actuator-zone- or boundary-condition-based CFD model. Lamkin et al. [10] and later Lamkin et al. [11] built upon this work to model the core flow of a high-bypass turbofan while optimizing the internal and external shape of the propulsor. Abdul Kaiyoom et al. [12] used the MACH-aero framework to simultaneously optimize the geometry of a wing and propulsor installed both under and over the wing to form a better comparison between the merits of each configuration.

To study the potential benefits of BLI, other work has used aerodynamic shape optimization with BLI configurations. Gray and Martins [13] and later Yildirim et al. [14] studied the benefits of a tail cone thruster with BLI for the STARC-ABL concept. The later study by Yildirim et al. [14] found a shaft power savings of about 11% to 16% for the BLI configuration when compared to the non-BLI baseline. Lauer and Ansell [15] similarly optimized the shape of the wing and propulsor together both under and over the wing but with BLI using the 2-dimensional code CFD MSES. In this case, they found the under wing and overwing optimized designs performed within 2% of each other.

Despite the previous work that has been done, there remains a need to further refine the design of SUSAN's underwing mailslot propulsor to address the unique challenges of distributed BLI propulsion wing integration. To address this need here we apply aerodynamic shape optimization to design SUSAN's mailslot propulsors. Through this

refined design we aim to provide a better benchmark for the performance of a mailslot and BLI mailslot design relative to a conventional configuration.

II. Methods

A. Geometry

In this paper we study two distinct geometries, the first is a mailslot nacelle isolated from the wing and the second is a mailslot nacelle mounted under the wing for BLI. Throughout this paper we refer to the first configuration as "mailslot" and the second as "BLI mailslot". In both cases, we make the following simplifications. First, our mailslot geometry has no sweep and each propulsor is identical. This allows us to design a single propulsor that is repeated to form the whole array of propulsors in the mailslot. Additionally, we impose left-right symmetry on the geometry. In the case of the isolated mailslot propulsor we impose top-bottom symmetry as well. This makes optimizing the mailslot propulsor more tractable by simulating only a fraction of a single propulsor and deducing the rest from the symmetry. This is similar to the approach used by Schmollgruber et al. [5] to study a similar BLI wing mount geometry.

These geometries were generated and parameterized in OpenVSP [16] for use within our optimization model. The duct component is formed from a lofted set of square, super ellipses, and circular cross-sections . The external part of the nacelle and wing are an airfoil cross-section design to be coincident with the start and end of the duct. We used extensive linking within the OpenVSP model and additional OpenMDAO [17] components to make sure the components that form our cohesive geometry were moved in unison and no gaps were opened in the geometry.

The initial mailslot geometry was generated by hand based on the internal passage of a podded free-flying propulsor designed for the same thrust requirement from Chau et al. [18]. Our initial baseline design attempted to approximately match the area distribution of the podded propulsor. Manual iterations were done to extend the inlet and outlet to reduce the shocks and separation in the flow similar to the work done by Machado et al. [3]. This geometry was used as the starting point of our optimization studies. The optimizer-selected design variables changed the initial design drastically and eventually the design changes from our baseline were too large for our mesh warping algorithm to produce a valid mesh. Thus, we reconstructed a baseline line design and mesh around the result of our preliminary optimization. The setup of this preliminary optimization study was less refined, so here we focus on the final optimization setup and results that use the initial optimizations as the starting point. The progression of the baseline design is shown in Fig. 3 with the baseline design used for this study.

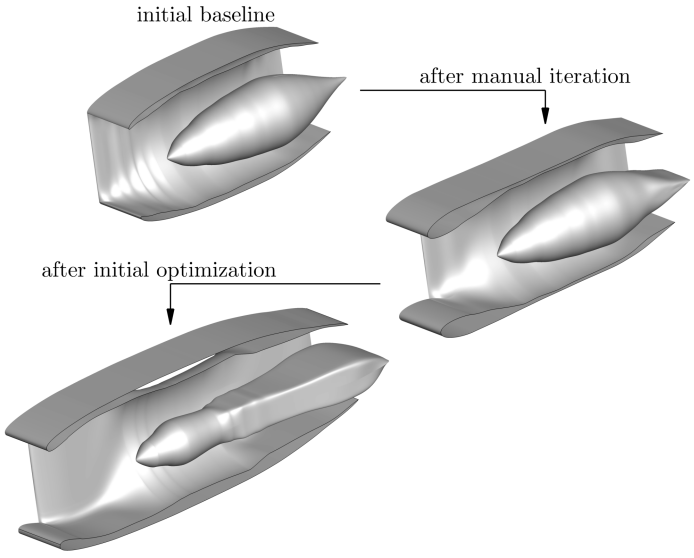


Fig. 3 The progression of the baseline mailslot design used in this study. A single propulsor is shown with half the nacelle cutaway for clarity.

Similarly, before we could optimize the BLI mailslot design we first needed to create the baseline configuration. Although unintentional, the design of the baseline BLI mailslot followed a similar trajectory as the mailslot-only design. To create the initial design, we combined an intermediate result for the optimized isolated mailslot with an airfoil section from the SUSAN geometry. The airfoil cross-section used to represent the wing was taken from the most inboard propulsor station. We chose the most inboard section of the propulsor array because this station had the largest PAI effects in a prior study by Machado et al. [8]. We modified the airfoil such that its trailing edge aligned with the exit of the mailslot duct. After an initial hand analysis showed strong shocks, we moved the wing down relative to the propulsor to flatten the top of the wing section and reduce the distance from the top of the airfoil to the trailing edge. Similar to the mailslot optimization, this initial design was modified so heavily by the optimizer that mesh warping failures prevented the optimizer from progressing. As a result, an intermediate design of the optimization had to be used as the new baseline for this study. Again, in this paper we will focus on the final optimization that yields the final optimized BLI mailslot geometry. The progression of the baseline BLI mailslot design is shown in Fig. 4.

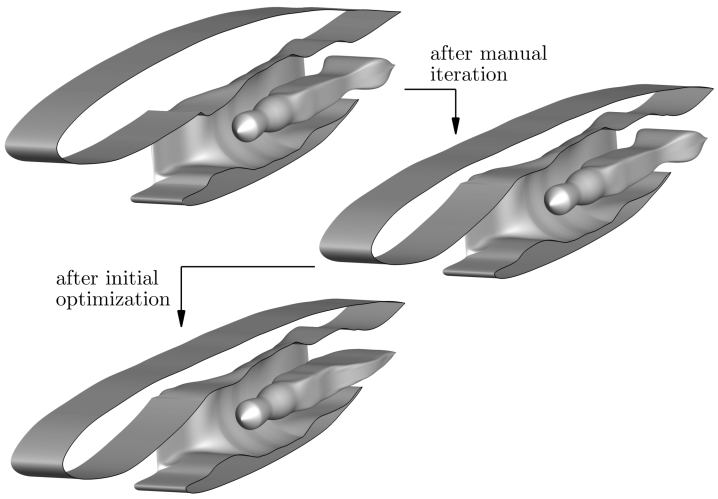


Fig. 4 Progression of the baseline BLI mailslot design in this study. A single propulsor is shown with half the nacelle and wing cutaway for clarity.

III. CFD Analysis

In both cases, we analyze the propulsors at SUSAN's top-of-climb flight condition, Mach 0.8 at an altitude of 35000 ft (10668 m). The fluid motion in and around the propulsor is described by the steady-state 3-dimensional RANS equations. We used ADflow [19], an open-source CFD solver, to solve the RANS equations. In addition to an efficient approximate Newton–Krylov (ANK) solver [20], to compute design variable sensitivities ADflow also has an adjoint solver.

The wall boundary conditions model the propulsor surface as viscous walls. We selected the Spalart–Allmaras (SA)[21] turbulence model to use in our simulation. At the outer rim of the mesh, we use a far-field boundary condition. To reduce the computational cost as much as possible we apply symmetry planes where possible. For the mailslot configuration, the mesh only includes a quarter of a single propulsor geometry. For the BLI mailslot configuration, the mesh induces half of the mailslot nacelle and wing. In both cases, we use symmetry planes on the right and left sides of the mesh to model the impact of the whole propulsor and the connected adjacent propulsors on either side. In Fig. 5 the quarter mesh has been repeated to show a representation of the entire mailslot propulsor geometry.

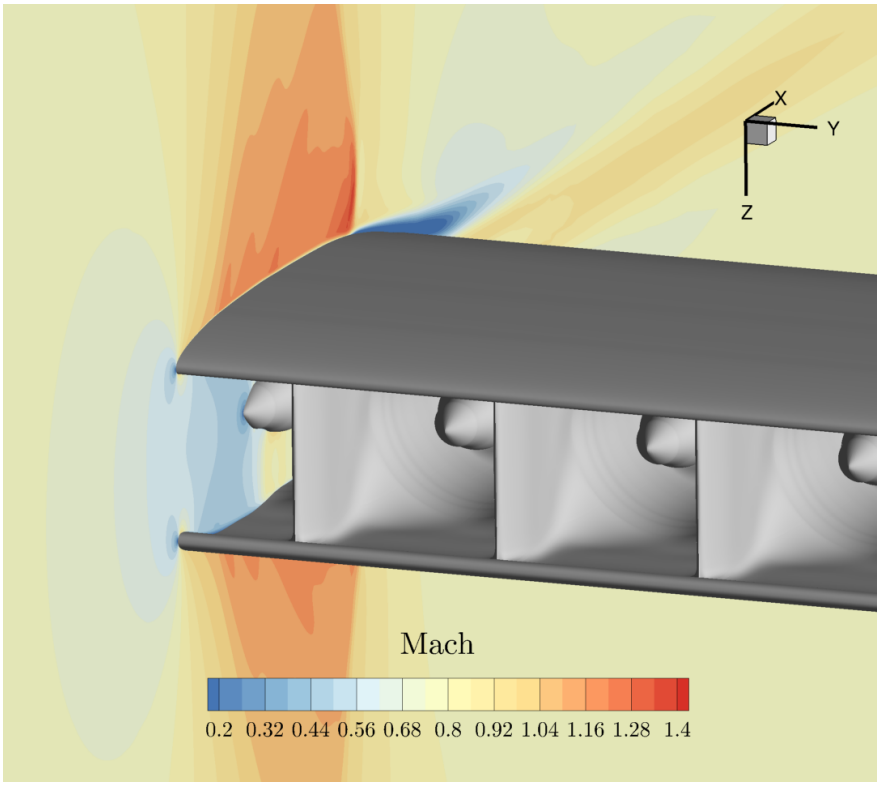


Fig. 5 ADflow is used to solve for the flow of a quarter mesh with symmetry planes that account for the influence of the entire geometry.

To model the influence of the motor's two fans on the flow we use the actuator zone method. In this method, the force of the fan is distributed over the volume of the fan disk as momentum source terms. We use the methodology of Gray and Martins [13] to measure flow power by integrating the force vector dotted with the velocity vector in each cell,

$$\mathcal{P} = \iiint_{\text{AZ}} \left(\vec{U}(\vec{x}) \cdot \vec{f}(\vec{x}) \right) d\vec{x}. \tag{1}$$

The force vector, $\vec{f}$, is set by the actuator disk model, but the local velocity $\vec{V}$ is determined by the flow field solution.

In addition to the force, the actuator zone also adds heat to the volume of the flow to account for the losses during compression. In contrast to the work done on coupled cycle and aerodynamic shape optimization [9–12] here we do not update the heat addition based on the flow properties to reduce the complexity of our optimization model. To estimate the heat addition to the flow we took the regression for the adiabatic efficiency of Gray and Martins [13],

$$\eta_a = 1.066 - 0.0866\text{FPR},$$

and applied our target fan pressure ratio to compute η_a. We then computed the heat addition, Q, to our model based on an estimate of the flow power, $\mathcal{P}_{\text{flow, est}}$, according to

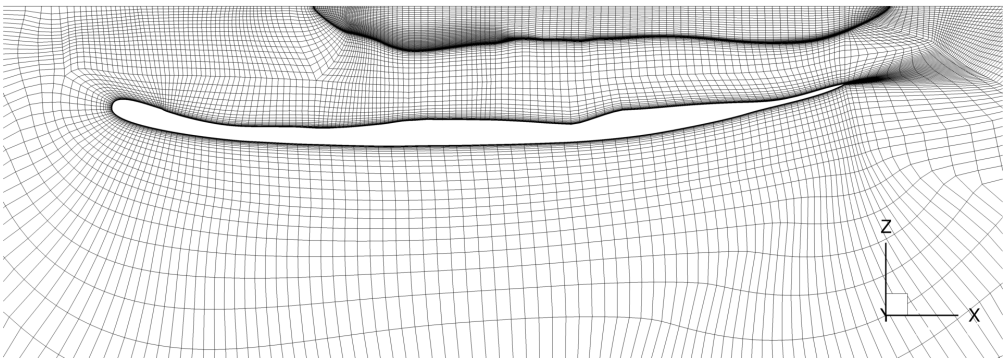
$$Q = \mathcal{P}_{\text{flow, est}}/\eta_a - \mathcal{P}_{\text{flow, est}}.$$

The resulting Q is evenly split over both actuator zones.

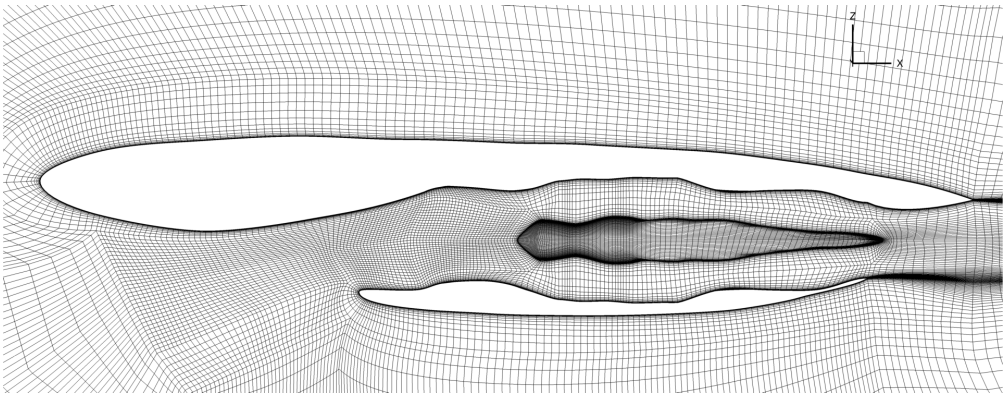
A. Mesh

We used Pointwise to create structured multi-block meshes for the mailslot and BLI mailslot geometries as shown in Fig. 6. The finest grid levels all had an off-wall spacing of 2.5e-6 which resulted in a $y^+ \approx 1$ over the surface. We created multi-block meshes so that it would be easy to create coarser meshes from the final meshes by simply removing every other grid point. These coarser meshes were used to create successively more expensive optimization problems.

For the mailslot configuration, the meshes have, 36 thousand, 300 thousand, and 2.4 million cells. For the BLI mailslot configuration the meshes have 100 thousand, 800 thousand, and 6.2 million cells. For the BLI mailslot we also made a addition grid with 2.5 million cells by coarsening the 6.2 million cell mesh by $1/\sqrt{2}$ in every direction except on the upper wing surface in stream wise direction. This mesh was constructed to reduce optimization time of the most refined BLI mailslot.



(a) Mailslot propulsor 300 thousand cell mesh



(b) BLI mailslot propulsor 800 thousand cell mesh

Fig. 6 Intermediate resolution multi-block meshes for each configuration. The finest mesh is twice as fine in every direction and the coarsest is twice as coarse in every direction.

B. Mesh warping

For each design iteration, the baseline mesh is warped to fit the surface of the new design. We use the IDWarp [22] package to create the warped volume meshes for each candidate design. This method propagates the deformations of the surface into the volume by weighting the deformation contributions of the surface nodes on the volume nodes according to their distance from each other. To make this method more robust for our use case we had to increase the exponential coefficients, a and b, of the equation used to assign the weights to each node. This increased the relative weight of the nodes closest to each point and consequently helped reduce mesh failures from small regions of the local surface pushing far into the volume of the mesh. This mode of mesh failure was particularly common at the trailing edge of the duct. To prevent symmetry plane warping errors we also needed to make an additional modification. When two symmetry planes face each other in IDWarp, one is applied to create a mirrored set of points and then the second is applied to mirror the original and mirrored points. This creates an effective geometry that is unbalanced and thus the points at one of the symmetry planes will not necessarily stay on the symmetry plane depending on the deformations of the surface. To reduce this error, we added additional fictitious symmetry planes offset from the mesh to add more sets of mirrored points. This resulted in a large reduction in the warping error. In the optimized design the largest departure from the symmetry plane was on the order of 1/100th of a degree, which we found sufficient for our use.

C. Thrust-drag bookkeeping

The thrust and drag decomposition we use here differs from the typical decomposition where only the forces external to the nacelle duct are bookkept as drag. Instead, we follow the approach of Gray et al. [23] and integrate the aerodynamic loads over all the exposed area. We then decompose the resulting force into a force parallel with the incoming flow, drag D, perpendicular to the flow opposite the ground direction, lift L , and lastly perpendicular to drag and lift, side force. Similarly, we split the total force applied to both actuator zones, $F_{\text{az,total}}$, into components parallel and perpendicular to the incoming flow. The component perpendicular to the flow is added to the lift resulting in the equation for net lift, L_{net}, of

$$L_{\text{net}} = F_{\text{az,total}} sin(\alpha) + L. \tag{2}$$

Likewise, we take the component of the applied force parallel to the flow and subtract the drag to compute net thrust,T_{net}, as shown in Eq. 3.

$$T_{\text{net}} = F_{\text{az,total}} cos(\alpha) - D \tag{3}$$

Combining the drag and thrust into a net thrust target allows the optimizer to take advantage of power savings due to a reduction in propulsor drag.

IV. Optimization Problem

Table 1 shows the objective, design variables, and constraints of the optimization problem being solved. The additional design variables and constraints specific to the BLI mailslot optimization case are highlighted in blue.

The extended design structure matrix (XDSM) in Fig. 7 describes the model we created in OpenMDAO [17] to analyze and optimize the design of our propulsors. OpenMDAO provides the framework for connecting different components of our model and propagation of the sensitivities through the entire model. At each iteration, the design variables are selected by the sequential least-squares quadratic programming (SLSQP) optimizer from the pyOptSparse package [24]. Utility functions constructed in OpenMDAO then translate the control point position and angle design variable data into the array of the control point positions used to parameterize the design in OpenVSP. Additional utility functions ensure the wing and nacelle surfaces always remain coincident with the duct inlet and outlet respectively. The geometric design parameters are then passed into OpenVSP, which is incorporated in our model through pyGeo [25], to generate a surface mesh of the candidate design. Using the OpenVSP Python interface and the OpenVSP wrapper of pyGeo, we can set parameters and get sensitivities from within our optimization loop. To produce the volume mesh needed by ADflow, IDWarp uses the updated surface mesh from OpenVSP to warp the initial volume so that the surface modifications are propagated into the mesh [22]. We then scale up the size of the mesh based on the scale factor design variable in OpenMDAO. Next in the optimization loop, the mesh representing the current design along with the aerodynamic design parameters (angle of attack and fan thrust) are evaluated by ADflow. MPhys [26] provides the existing OpenMDAO wrapper for ADflow that we used in our model. A final OpenMDAO component takes in the results of the CFD analysis to compute the total shaft power of SUSAN's 16 propulsor array as well as the net thrust.

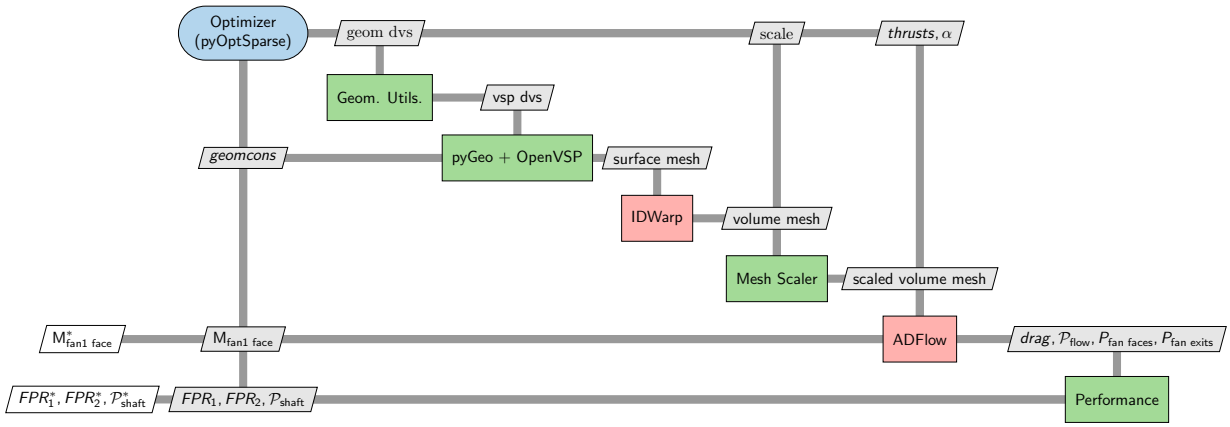


Fig. 7 The XDSM of the model used to optimize the propulsor geometries.

Table 1 Description of the propulsor design optimization problems. The values in blue are specific to the BLI mailslot case while values in black are common to both.

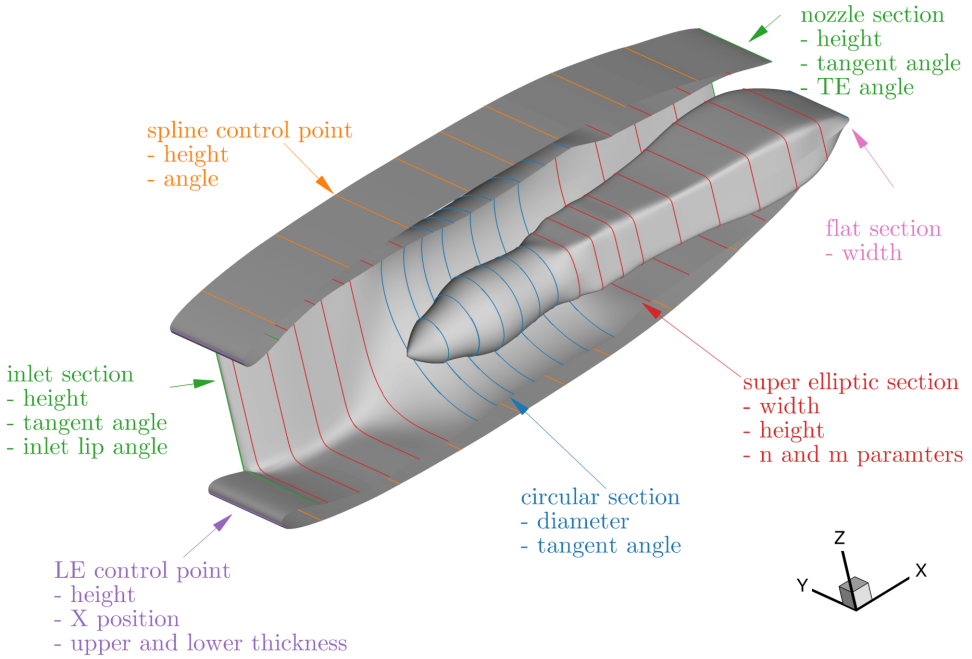
	Parameters	Description	Quantity
min	$\mathcal{P}_{\text{flow}}$	Power applied to the propulsor's fans	1
w.r.t.	T_{fan}	The thrust applied to each fan's actuator zone	2
	α	angle of attack	1
	scale	scale of the wing and propulsor	2
	$D_{\text{cross-section}}$	parameters for the duct cross-sections	55
	$H_{\text{cross-section}}$	parameters for the hub cross-sections	50
	D_{length}	Length from splitter to fan and from fan exit to nozzle	2
	H_{length}	Length from throat to hub end and from spinner to fan face	2
	$D_{\text{Z offset}}$	Offset of the inlet and nozzle cross-sections upwards	11
	$H_{\text{Z offset}}$	Offset of the aft hub cross-sections upwards	2
	N_{cp}	y positions and tangent angles of external nacelle spline control points	22
	W_{cp}	y positions of and tangent angles of external wing spline control points	31
		total	135/180
s.t.	$T_{\text{net}} = T^*$	The net thrust of the propulsor is equal to the target thrust	1
	$FPR = \sqrt{1.25}$	Each fan has a pressure ratio of $\sqrt{1.25}$	2
	$M_{\text{fan1}} \leq 0.6$	The fan face Mach number of the first fan is less than or equal to 0.6	1
	$L_{\text{net}}/\text{span} \leq l^*$	The sectional lift is greater than or equal to the lift required	1
	$t_{\text{motors}} \geq 0.3 D_{fan,0}$	The hub is large enough to fit the estimated motor size	10
	$t_{\text{LE}} \geq t_{\text{LE},0}$	The leading edge thickness is greater than or equal the initial	1,1
	$t_{\text{nacelle}} \geq 0.05m$	The nacelle thickness is greater than or equal 0.05m	30,40
	$t_{\text{nacelle,TE}} \geq t_{\text{nacelle,TE},0}$	The nacelle trailing edge thickness is greater or equal the initial	10
	$t_{\text{wing,TE}} \geq 0.3 t_{\text{wing,TE},0}$	The wing thickness near the trailing edge is at least 30% the initial	40
	$t_{\text{wing}} \geq 0.85 t_{\text{wing},0}$	The airfoil thickness at the front of the wing is at least 85% the original	12
	$t_{\text{duct,side clearance}} \geq 0$	The duct cannot be wider than the inlet and nozzle	10
	$t_{\text{duct}} \geq 0.5 t_{\text{duct},0}$	The duct thickness cannot be less than 50% the initial	20,20
	$t_{\text{duct,side}} \geq 0.66 t_{\text{duct,side},0}$	The duct side thickness cannot be less than 66% the initial	20
	$t_{\text{nozzle}} \geq 0.75 t_{\text{nozzle},0}$	The nozzle bottom thickness cannot be less than 75% the initial	2,5
	$\Delta D_{\text{height}} \leq 0.066$	The change in height between duct cross-section is less than 0.066	17
	$\Delta H_{\text{height}} \geq -0.05$	The change in height between hub cross-section is greater than -0.05	14
	$0.02 \leq \Delta L_{\text{aft}} \leq 0.04$	The end of the duct and the end of the nacelle must remain close	1
	$-0.06 \leq \Delta y_{\text{inlet}} \leq 0.06$	The angle of the duct inlet is limited	1
		total	141/259

A. Objective function

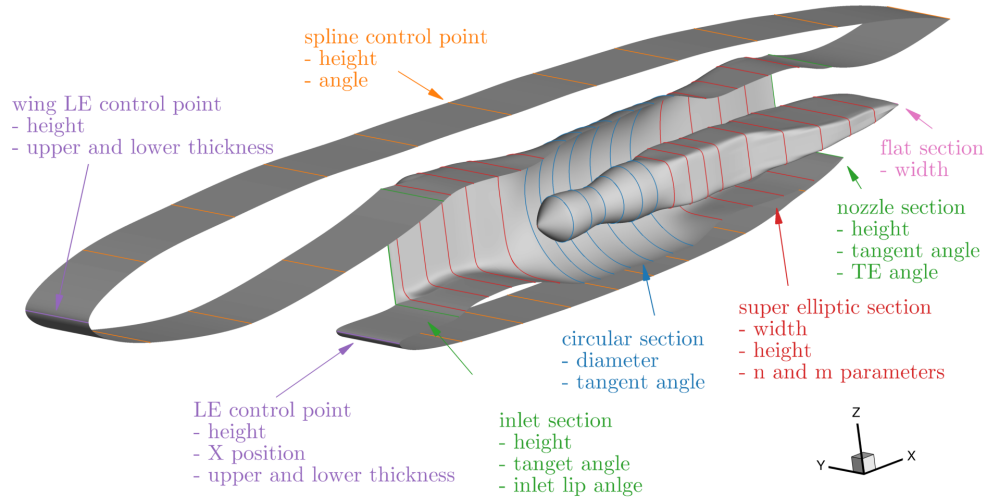
The objective of our optimization problem is the total flow power required to drive the propulsor fans. The flow power is the mechanical component of the shaft power and consequently minimizing flow power in our model is the same as minimizing shaft power. The total flow power is computed by taking the flow power of the CFD simulation and multiplying it by 4 for the quarter simulation and 2 for a half simulation to get the flow power of one propulsor. Since SUSAN has 16 propulsors, we then multiply the propulsor flow power by 16 to get the total flow power.

B. Design variables

The design variables control the shape of the geometry and the operating conditions of the fans and wing. A subset of parameters defining the duct, hub, nacelle, and wing geometry are exposed by the OpenVSP wrapper for use as geometric design variables. The hub and the duct of the propulsor are created from a set of lofted cross-sections while the nacelle and wing are formed from spline control points. Figure 8 shows the cross-sections and control points of the mailslot and BLI mailslot designs as well as the set of parameters that are exposed as design variables in our optimization.



(a) Mailslot sections and design variables



(b) BLI mailslot sections and design variables

Fig. 8 Both the mailslot and BLI mailslot are formed from cross-sections and control points. Each cross-section has a set of parameters that are used as design variables in the optimization.

The diameter, width, and height of the duct and hub cross-sections are set by design variables, with the exception of the inlet and nozzle, which have a set width. The angles of the surface at these cross-sections provide the optimizer with further shape control. Not all sections have angle design variables and some are instead set to preserve the C2 surface continuity. Particularly, the mostly rectangular sections were more streamlined with a different tangent angle along each side making it better to remove the set tangent angle parameterization.

The cross-sectional shape of the super elliptic sections can be controlled by adjusting the m and n super ellipses parameters. These parameters are the coefficients in the super ellipse equation,

$$\left|\frac{x}{a}\right|^m + \left|\frac{y}{b}\right|^n = 1.$$

When $m = n = 2$ then the equation matches the equation for a circle. As m and n become larger the resulting curve becomes more rectangular. By using different values for m and n the curvature of the cross-section can be shifted. Figure 9 shows these trends graphically. For the BLI mailslot case, at the inlet and nozzle of the duct and at the tail of the hub the cross-sections can be shifted upwards in the Z direction by design variables to create top-bottom asymmetry.

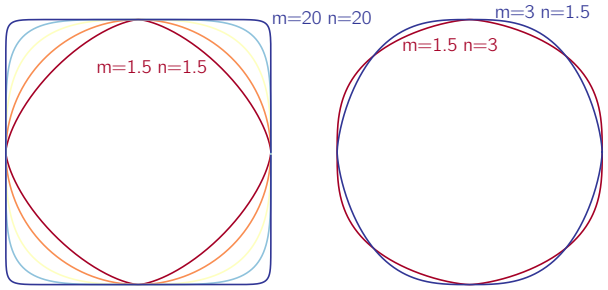


Fig. 9 By adjusting the super ellipse parameters m and n the cross-sections can be made more circular or rectangular.

The length of the duct's inlet and nozzle section and the hub's spinner and tail are also design variables. These design variables are made by moving the x-position of a set of cross-sections as a group. Figure 10 shows the length design variables on the mailslot design, but both the mailslot and BLI mailslot have these design variables.

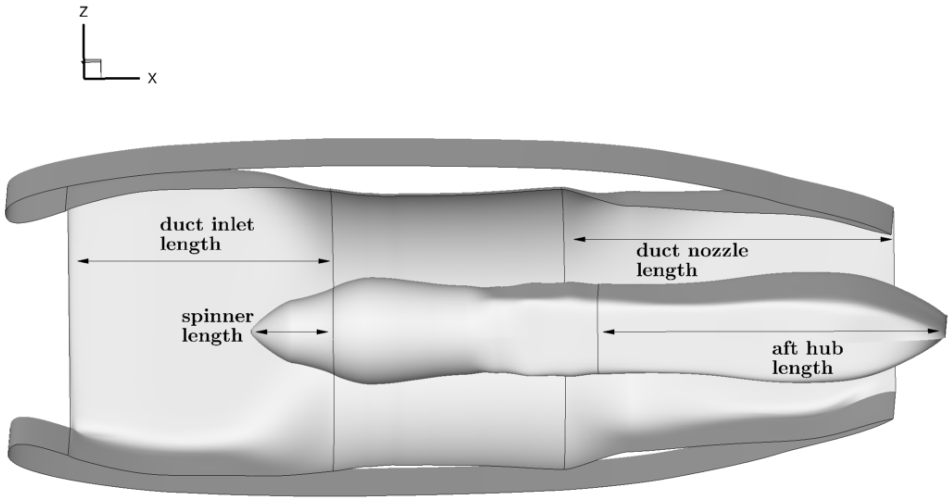


Fig. 10 The length design variables for the duct and hub, which are used for both the mailslot and BLI mailslot optimizations.

The wing and external nacelle surfaces are parameterized with the position and angle of the control points of Bezier splines. This includes the leading edge of the wing and nacelle, which are parameterized to always have an angle of 90° but can have a variable thickness. The nacelle leading edge also has the additional X-position design variable to lengthen the nacelle lip.

The scale variable uniformly scales up the size of the entire propulsor. The motivation for including this variable was to allow the optimizer to scale the propulsor to meet the net thrust requirement as was done by hand in earlier studies by Machado et al. [3]. In the podded propulsor case, the optimizer could increase the diameter of all the cross-sections. However, the symmetry planes prevent the optimizer from increasing the width of the inlet and nozzle directly, but by scaling the entire mesh up, the width of these sections (and everything else) can be increased.

In addition to the geometric variables, the optimizer also has control over some aerodynamic variables. The force applied to each of the actuator zones is a design variable. Additionally, the angle of attack is a design variable for the BLI mailslot optimization problem.

C. Constraints

The most important constraint is arguably the net thrust. The net thrust target ensures the optimized propulsor can fulfill its role by meeting the thrust required at the top-of-climb condition for SUSAN. By posing the constraint on the net thrust rather than the gross thrust the optimizer is allowed to reduce the applied thrust if it can reduce the drag of the propulsor. This creates a large incentive for the optimizer to reduce the drag of the propulsor. For the BLI mailslot configuration, the viscous drag of the baseline wing is subtracted from the thrust target because it is accounted for in the drag of the CFD analysis. The fan pressure ratio (FPR) constraints on the fan enforce that the final design matches the required FPR of the SUSAN design. In SUSAN's propulsors the overall all FPR of 1.25 is evenly distributed between two fan stages contained within each propulsor.. A fan face Mach number constraint ensures that the inflow does not fall outside the operating range of the first fan. For the BLI mailslot configuration, the optimizer must also meet the lift constraint for that section of the wing. The sectional lift constraint was found by assuming lift equals weight at the top-of-climb condition and then determining the sectional lift at the first propulsor's span-wise location by assuming an elliptical lift distribution. The net lift, as defined in Eq. 2, is divided by the span of the wing section to determine the sectional lift from the CFD simulation.

The complex geometry of these two configurations has also led to a complex set of geometric constraints to ensure the geometry remains valid. The set of thickness constraints is shown graphically in Fig. 11

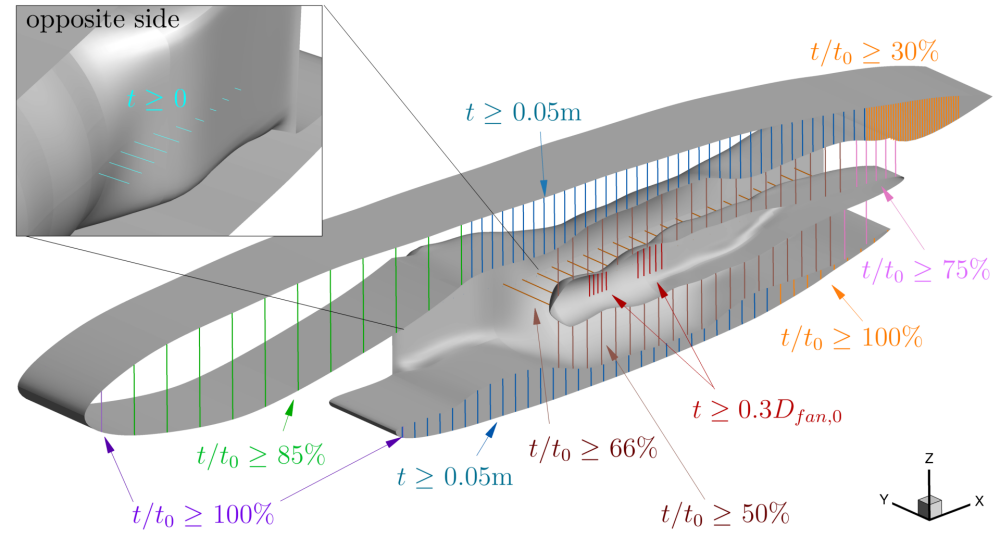


Fig. 11 The colored lines show the thickness constraints of the optimization problem. The thickness constraints prevent the geometry from becoming unrealistically thin and help prevent the optimizer from selecting designs that break the mesh warping too often.

The geometric constraints were created to serve two separate purposes the first is to prevent the optimizer from

making the design of the propulsors unrealistic. The motor thickness constraints ensure that a motor sized to fit in the initial design will also fit in the optimized design. The size of the motor was calculated based on the rule of thumb that the motor will be approximately 30% the diameter of the fan blade. Note that we did not attempt to resize the motor based on the updated size of the fan throughout the optimization, but instead used a consistent value that reflects the approximate size of the baseline motor. The leading edge radius constraints help prevent the optimizer from making the design overly specialized for this single analysis condition by reducing the leading edge radius. The thickness of the nacelle and wing section above the duct is constrained to be greater than or equal to the minimum thickness of the podded propulsor which was found to be 0.05 m. At the trailing edge, we constrain the optimizer to retain at least the initial thickness of the nacelle and at least 30% of the original thickness of the wing. In front of the duct, we also constrain the wing thickness to be at least 85% of the baseline thickness.

In addition to the constraints used to prevent the design from getting too thin, additional constraints were added with the intent to prevent the optimizer from exploring designs that caused mesh warping failures or were pointless to evaluate. The constraint on ΔD_{height} and Δy_{inlet} helps smooth out the design of the duct. The intent behind this constraint was to prevent intermediate designs with excessive separation in the inlet of the BLI mailslot design. Similarly, the constraints on ΔH_{height} help prevent designs with separation on the hub. Such designs are difficult to converge and undesirable. Finally, the constraint on the difference between L_{nozzle} and $L_{\text{aft hub}}$ helps prevent excessive skewing in the mesh warping that can lead to failures.

V. Results

In all cases, the optimizer produced a design that satisfies the constraints of the design problem. Table 2 shows the flow power for each of the optimized cases. Relative to an optimized podded propulsor the flow power of the optimized mailslot propulsors was slightly higher. The optimized podded propulsor design used in this section is from the work of Chau et al. [18].

We solved each optimization problem on successively finer CFD meshes. Bons and Martins [27] showed for an aerostuctural optimization problem this multilevel approach can reduce the overall walltime of the optimization by 40%. However, we found this strategy to be most valuable for quick iteration on the optimization setup. Furthermore, the design exploration of the early optimization is easiest on a coarse mesh, which is less prone to mesh warping failures. In the mailslot case, we were able solve the optimization on the finest, 2.4 million cell, mesh level. However for the BLI mailslot design we were only able to reach the 2.5 million cell mesh. As the mesh is refined the performance gains from optimizing again diminish. When taking the BLI mailslot design optimized on the 800 thousand cell mesh and then re-optimizing on the 2.5 million cell mesh, the the flow power reduced by only 0.2 MW. We analyzed the final optimized BLI mailslot design on the 6.2 million cell mesh and the results of the fine mesh simulation would not change the values of Table 2 to the precision shown and the design still meets all constraints. In Section VI.C when comparing the relative values of individual optimized propulsors, the finest mesh analysis results are used for all propulsors.

Table 2 The flow power and key constraint values for each of the optimized propulsors. When present the imperial representation is in parentheses. The BLI mailslot was designed to produce less excess thrust thrust because the viscous drag of the wing section is accounted for in the drag of the propulsor.

	flow power MW (hp)	net thrust kN (lbf)	1st fan face Mach
podded	**9.6** (12900)	33 (7400)	0.60
mailslot	**10.5** (14100)	33 (7400)	0.60
BLI mailslot	**11.0** (14800)	30 (6700)	0.60

A. Mailslot

The design obtained from the optimization of the mailslot is shown in Fig. 12 with Mach contours. The optimizer was able to remove the shocks from the external and internal flow as well as the excessive flow separation. However, the optimized design still has some flow separation at the aft portion of the nacelle and hub. The flow inside the duct of the propulsor is subsonic while the external flow reaches supersonic speeds as it moves over the nacelle.

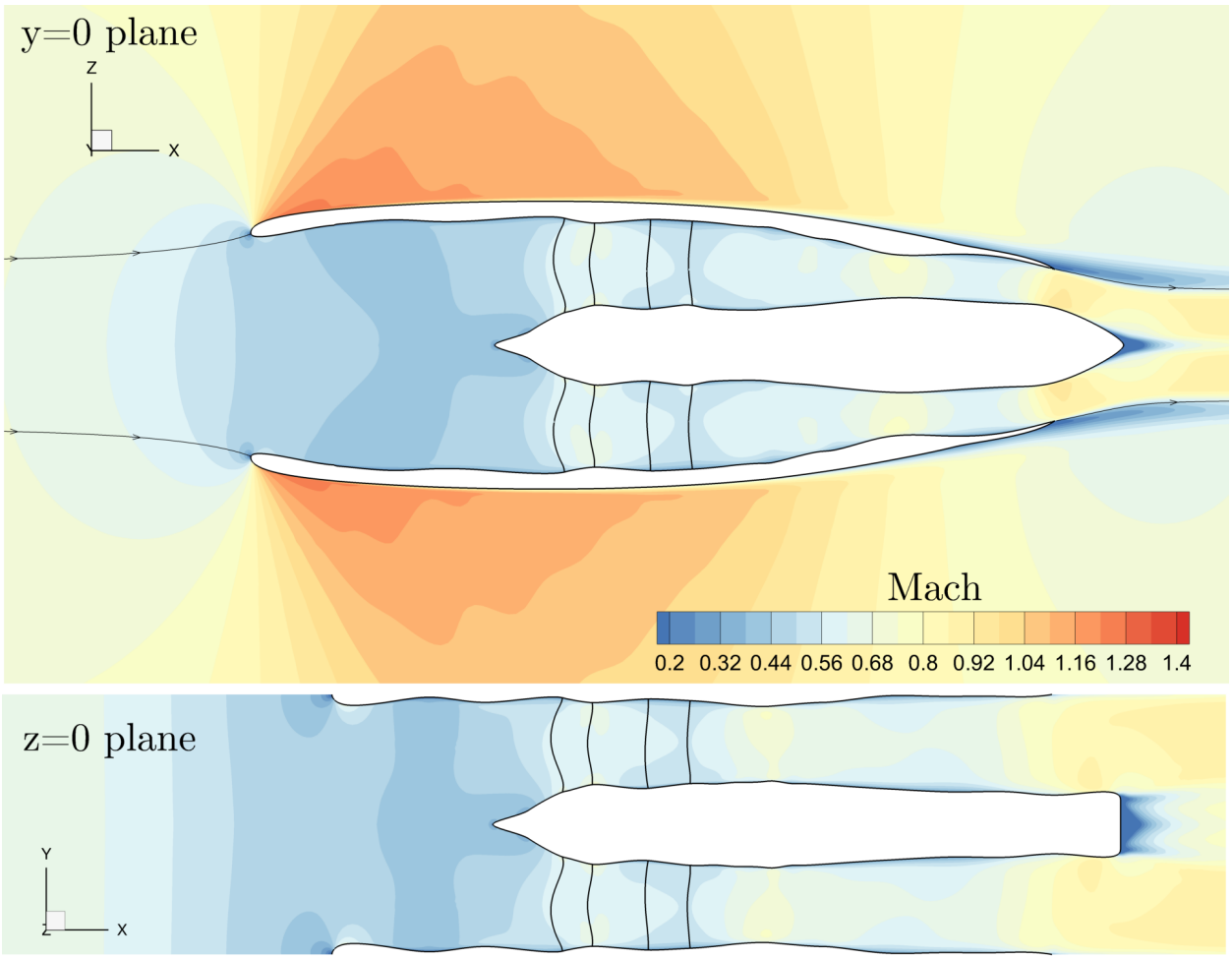


Fig. 12 Mach contours of the optimized mailslot design on the 2.4 million cell mesh. The actuator zones are outlined with black lines and stagnation streamlines show the capture area.

The most notable feature of the optimized design is its length relative to the podded propulsor. The optimized mailslot design is over 2 times longer than the optimized podded design. The design variables for the length of the duct and hub are all at their maximum value. Additionally, the whole geometry is scaled up by a factor of 14% by the scale design variable. The super elliptic sections of the hub grow to have a greater height than width in the aft portion. In the $y = 0$ plane, the height distribution of the propulsor hub is similar to that of a typical podded propulsor, with the maximum height point near the nozzle. In the $z = 0$ plane, the hub does not come back to a point, but rather remains a more consistent width after the second fan. However, this is limited by the bounds of the hub's width design variables which are nearly all at their lower bound. The nacelle is at or near the lower thickness bounds along its length. This makes sense as removing thickness helps weaken the external shocks of the nacelle. Similarly, the leading edge radius constraint is at its lower bound as well as the first of the motor thickness constraints.

The super elliptic sections of the optimized hub and duct are highly rectangular, as shown in Fig. 13. For the duct, the transition from rectangular sections to circular happens over a similar distance as the transition from circular sections back to rectangular.

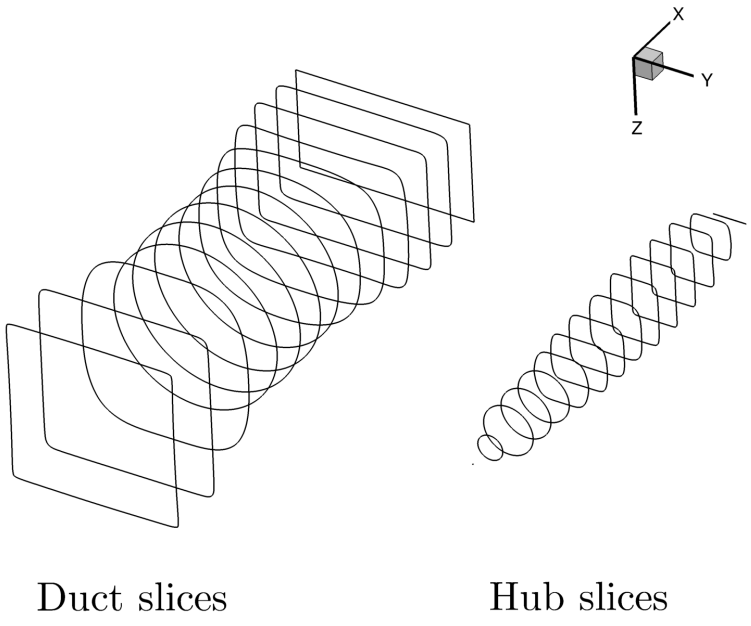


Fig. 13 Slices through the mailslot's duct and hub show how the cross-sectional shape evolves over their length.

B. BLI mailslot

The design obtained from the optimization of the BLI mailslot geometry is shown in Fig. 14 with contours of Mach number. Once again the optimizer was able to remove the shocks present in the baseline design and reduce the separation. The flow inside the duct is also all subsonic, with a noticeable region of low-speed flow along the top wall of the inlet and nacelle duct. Like the mailslot design, the optimized BLI mailslot design is very long. The aft portion of the hub and duct were stretched to their maximum length by the optimizer. The front of the nacelle was also stretched to nearly its maximum length leading to a long inlet. The hub of the optimized design has the largest height just aft of the second fan and maintains a large thickness until the nozzle. The width of the hub on the other hand, is similar to the mailslot design and is mostly constant along the length. The optimized duct inlet grows in height while contracting along the width direction. The z-offset design variable at the duct inlet produces an asymmetry in the inlet causing the inlet to move up into the wing more. The height of the duct has small variations near the middle. Immediately before and after the circular cross-sections there is a decrease in the duct height as the cross-sections transition to be more rectangular. Additionally, before each fan face there is an increase in diameter. The wing and nacelle are at or near the minimum thickness along their length. The motor could not be moved upward into the wing more without displacing the upper surface. This appears to reduce the distance from the crest of the airfoil to its trailing edge, which must also act as the trailing edge of the propulsor. Moving the motor further up into the wing makes the curvature before the inlet greater and allows for more diffusion as well. Relative to the centerline of the propulsor, the chord line of the wing has been twisted to an angle of 3.2 degrees. At the optimized farfield angle of attack of -2.1 degrees, the wing has an effective angle of attack of 1.1 degrees. The negative angle of attack also means that the thrust of the propulsor is pointing slightly downwards.

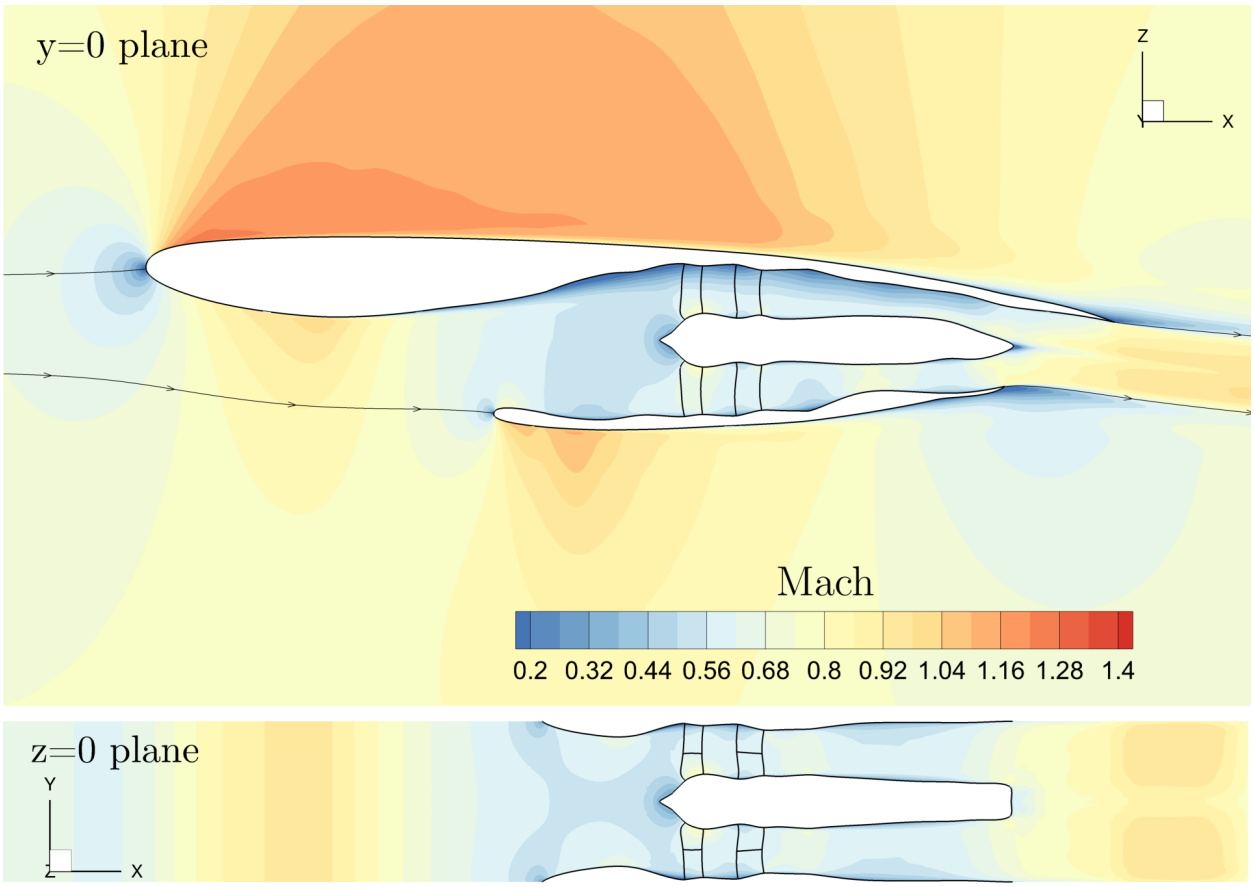


Fig. 14 The Mach contours of the optimized BLI design on the 2.5 million cell mesh. The actuator zones are outlined with black lines and stagnation streamlines show the capture area.

Figure 15 shows the shape along the length of the hub and duct. The transition from rectangular to circular happens gradually at both the inlet and the nozzle. The transition from circle to rectangle is more abrupt on the hub which has mostly rectangular sections.

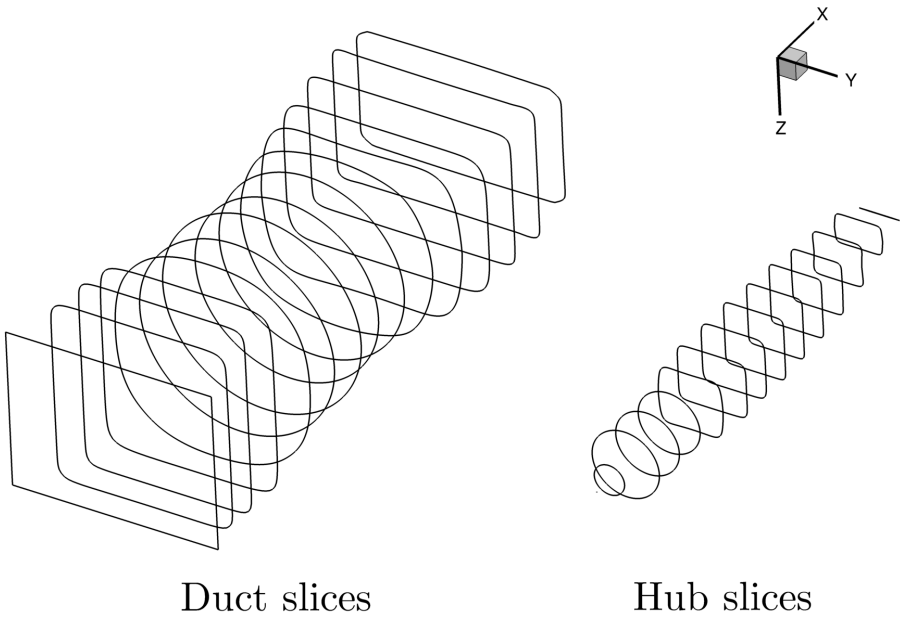


Fig. 15 The slices of the BLI mailslot design's duct and hub show how the cross-sectional shape evolves over their length.

VI. Discussion

A. Averaged flow properties

Using the volume solutions of the optimized designs, we took the area and the average of the pressure, and Mach number at each along the passage of the nacelle duct. For the pressure we computed an area average while for the Mach number we computed a mass-flow-based average. Figure 16 shows the 1-dimensional distribution of these three quantities over the length of the duct for the podded propulsor, optimized mailslot, and optimized BLI mailslot designs. When comparing these distributions we can identify some similarities and differences. As one would expect,the nozzle had the lowest area and highest Mach number for all propulsors. Additionally, at the nozzle the propulsors had a similar ratio of area to the first fan face; 0.72 for the podded and BLI mailslot and 0.74 for the mailslot. For both the mailslot and BLI mailslot designs the pressure after the second fan stays high until just before the nozzle. In contrast to the podded and BLI mailslot designs, the mailslot's inlet has a larger area relative to the first fan face. In the mailslot design the increase in Mach number due to the contraction from the inlet to the first fan is offset by a slower flow at the inlet. The mailslot design has a greater inlet pressure which slows the flow more before it enters the propulsor.

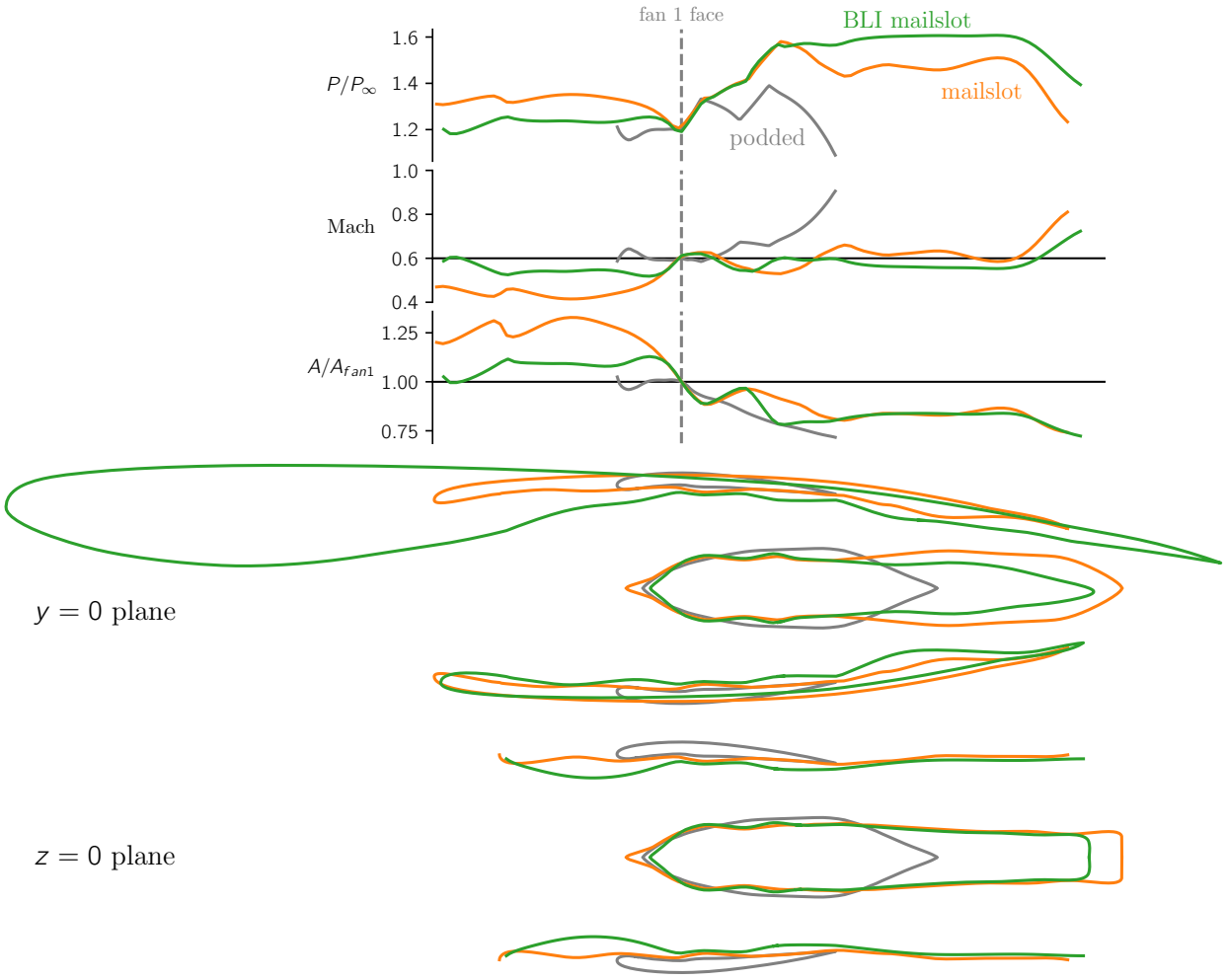


Fig. 16 Pressure, Mach, and area distribution as a function of stream-wise position. Underneath the distributions, the slices in the $y = 0$ and $z = 0$ planes show the shape of each propulsor.

B. Lengthening

For both mailslot designs the optimizer selected much longer hub and nacelle surfaces than the podded propulsor. We believe that the optimizer lengthened the nacelle to reduce the camber on the external nacelle surface. Furthermore, we believe this was necessary because a mailslot design with a similar sectional area distribution to a podded design will have a greater change in height. Figure 17 shows a comparison of the height and width of a podded propulsor to mailslot designs created by replacing the inlet and nozzle with rectangular cross sections that either match the area or the dimensions of the podded propulsor sections. Matching the sectional areas produces a notable difference in height between the cross-sections at the inlet and nozzle. This greater change in height leads to a larger camber on the external nacelle surface, which can lead to shocks or separation at transonic conditions. To have the same slope as the podded propulsor nozzle, the distance from the second fan exit to the nozzle of the mailslot design would have to increase by approximately 3 times. However, matching the height of the podded propulsor at the inlet and exit produces negative effects too. Figure 17 also shows the area ratios of the mailslot designs that match the area and height at the inlet and nozzle. Using the conditions at the fan faces and exits with the isentropic flow relations, we can estimate the Mach number at the inlet and nozzle for each of these hypothetical designs. When the height is matched, the flow at the inlet and nozzle of the resulting mailslot design would be slower due to the greater relative area. This is particularly bad at the nozzle where the area expansion prevents the increase in Mach number that we see in all the optimized designs.

This suggests that one reason the optimizer lengthened the designs is to address the geometric challenges of a mailslot design. Relative to the podded propulsor our optimized mailslot designs are about 4 times longer from the inlet to the first fan and from the second fan to the nozzle. The area ratio of the nozzle to the first fan face of the optimized designs are similar to the podded design and range from 0.72 to 0.74. However, at the inlet the area ratios differ. The optimized isolated mailslot has an inlet area ratio, 1.2., which is larger than the hypothetical area-matched design and smaller than a hypothetical height-matched design. On the other hand, the BLI mailslot design has an area ratio about equal to that of the podded propulsor.

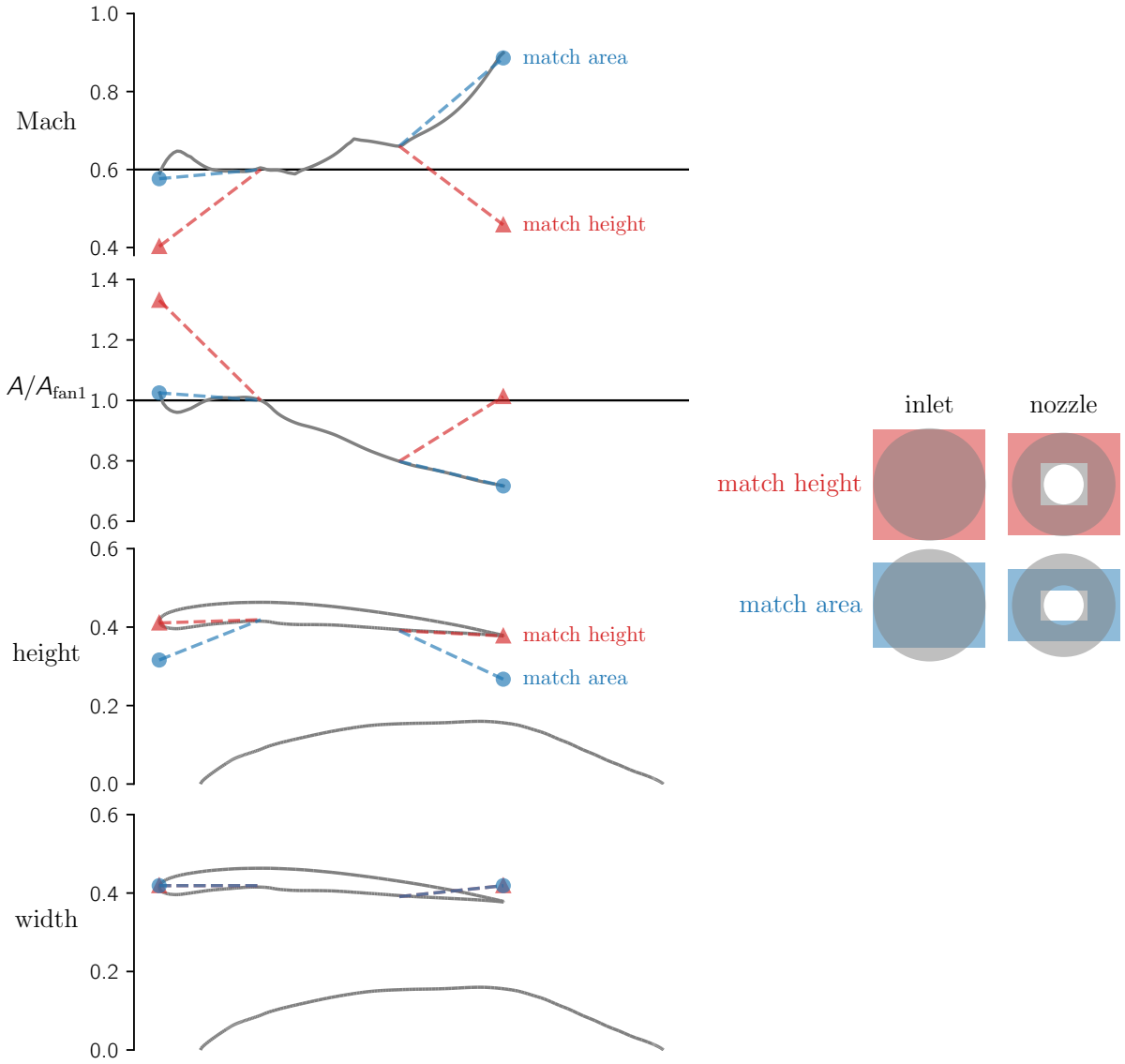


Fig. 17 A comparison of hypothetical rectangular cross-sections that match either the height or area of the podded propulsor's circular cross-sections. The dashed lines show how the geometric properties and the Mach number would change over the length relative to the optimized podded propulsor.

C. Relative performance

To gain further insight into these performance differences, we can decompose the integral equation of Eq. 1 into separate terms based on how the actuator zone method is implemented. First, we make a substitution for $\vec{f}$ based on

how the actuator zone model distributes the force,

$$\vec{f}(\vec{x}) = \frac{F_{\text{az}}}{V_{\text{az}}}\vec{n}_{\text{az}}.$$

F_{az} is the total force added to an actuator and $\hat{n_{\text{az}}}$ is the direction which force is applied. In our model, all the force of the actuators is applied along the fans' axis of rotation (simply the x-axis in this case). In Eq. 1, V_{az} is the volume of the actuator zones which the force is distributed over. In our CFD simulation, we have two distinct actuator zones and thus can break Equation 1 into an integral for each. Substituting for $\vec{f}$ and separating the integral results in Eq. 4.

$$\mathcal{P} = \frac{F_{\text{az1}}}{V_{\text{az1}}} \iiint_{\text{AZ1}} \left(\vec{U}(\vec{x}) \cdot \vec{n}_{\text{az1}}\right) d\vec{x} + \frac{F_{\text{az2}}}{V_{\text{az2}}} \iiint_{\text{AZ1}} \left(\vec{U}(\vec{x}) \cdot \vec{n}_{\text{az2}}\right) d\vec{x} \tag{4}$$

The $1/V_{\text{az}} \iiint_{\text{AZ}}() d\vec{x}$ operator represents a volume averaging over the actuator zones while the $\vec{U} \cdot \hat{n_{\text{az}}}$ integrand represents the velocity component at each point along the thrust axis. We are going to define the effective velocity, U_{eff}, as the result of this volume averaging of the velocity component along the axis of force,

$$U_{\text{eff}} = \frac{1}{V_{\text{az}}} \iiint_{\text{AZ}} \left(\vec{U}(\vec{x}) \cdot \vec{n}_{\text{az}}\right) d\vec{x}.$$

By substituting U_{eff} into Eq. 4, it simplifies to Eq. 5.

$$\mathcal{P}_{\text{flow}} = F_{\text{az1}} U_{\text{eff1}} + F_{\text{az2}} U_{\text{eff2}} \tag{5}$$

In the optimized designs the total force added to the actuator zones,$F_{\text{az,total}}$ must exceed the drag,D, by the target thrust, T^*, according to Eq. 3. The podded and mailslot analysis assumes no angle of attack and the optimized BLI mailslot design has an angle of attack of about -2°. Consequently, we can make the small angle approximation $(cos(\alpha) \approx 1)$ to produce,

$$F_{\text{az,total}} = (T^* + D).$$

Rewriting each force variable in Eq. 5 as $F_{\text{az,total}}$ multiplied by a thrust fraction, and then substituting for $F_{\text{az,total}}$ produces Eq. 6.

$$\mathcal{P}_{\text{flow}} = \underbrace{(T^* + D)}_{F_{\text{az,total}}} \underbrace{\left[\left(\frac{F_{\text{az1}}}{F_{\text{az,total}}}\right) U_{\text{eff1}} + \left(\frac{F_{\text{az2}}}{F_{\text{az,total}}}\right) U_{\text{eff2}}\right]}_{U_{\text{eff,total}}} \tag{6}$$

This new equation algebraically relates the flow power, $\mathcal{P}_{\text{flow}}$, target thrust, T^*, drag of the propulsor, D, and terms related to the velocity of the flow in the actuator zones. For each propulsor the U_{eff} terms represent the power cost for a given amount of thrust. The thrust fraction terms weigh the individual effective velocities to determine how efficiently the overall propulsor produces thrust. Table 3 lists the value of each component of Eq. 6 for the propulsors of each design.

Table 3 The thrust and effective velocities for each of the designs and fan actuator zones.

	total			fan 1		fan 2	
	force kN	$U_{\text{eff,total}}$ m/s	power kW	force%	U_{eff} m/s	force %	U_{eff} m/s
podded	3.1	193	598	52	181	48	205
mailslot	3.7	179	654	55	189	45	168
BLI mailslot	3.9	178	688	43	185	57	173

The total flow power per unit thrust, or $U_{\text{eff,total}}$, as shown in Table 2, of each of the designs is similar, about 180-190 m/s. Furthermore, because there is a slight reduction in $U_{\text{eff,total}}$ for the mailslot and BLI mailslot it is clear that the overall increase in power comes from the larger force applied. The similar $U_{\text{eff,total}}$ values imply that the velocity distributions in the optimized actuator zones are similar. At the entrance to the first fan all designs are at the upper limit of the fan face Mach number constraint, 0.6. Even though the BLI mailslot design ingests a region of slower flow,

the faster flow outside the boundary layer brings the average back up to 0.6. It is surprising that the podded propulsor design has a higher total $U_{\text{eff,total}}$ than the mailslot. One confounding factor is that the podded propulsor optimization did not have the additional spinner and duct length design variables and had a more restrictive lower bound on the hub diameters (80% baseline rather than 60%) [18]. It is possible that with these optimization modifications, the flow power per unit thrust of the podded propulsor would decrease.

The larger difference between the optimized designs is the difference in thrust they produce. The podded and mailslot designs have the same target net thrust, yet the mailslot design must produce more thrust to offset its higher drag. Initially one might think that a mailslot design would have less drag and thus less flow power because adjacent propulsors in a mailslot array share walls on the right and left side. At the fan cross-sections the external perimeter is about $2/\pi$ (64%) times less for the mailslot design since the external perimeter of the mailslot only has a top and bottom and the thickness is about the same. However, after re-examining our initial design of a mailslot propulsor we can start to see why we were unable to achieve a drag savings. Before manual iteration or initial optimization, relative to our podded propulsor our initial baseline design had 83% the external surface area of the podded design. The initial design fell well short of the 64% reduction in external area even with our initial insufficient lengthening of the nacelle. Furthermore, the wetted area savings were only on the exterior. Inside the nacelle the wetted area increased by 36% causing a total nacelle wetted area increase of 7%. In addition to the increase in wetted area, it can also be more difficult to manage the change in height and cross-section without separation as discussed in Subsection VI.B.

When we examine the contributions of viscous drag of the mailslot designs relative to the podded design as shown in Table 4 we can see that the viscous drag is greater both inside and outside the duct flow. Likewise, the pressure drag contributions of the mailslot designs are also greater than the podded propulsor. However, the drag of the podded propulsors does not incorporate any additional penalties from mounting 16 propulsors onto the wing. This contribution is also missing from the drag of the mailslot propulsor but is inherently accounted for in the BLI mailslot design.

Table 4 The drag contributions for a single propulsor of each optimized design.

	pressure drag (N)	internal viscous drag (N)	external viscous drag (N)	drag per propulsor (N)
podded	871	100	80	1050
mailslot	1300	178	125	1600
BLI mailslot	1610	212	157	1980

D. Distortion

Figure 18 compares the Mach number distribution across the first face fan. Although they each have the same mass-averaged Mach number, 0.6, the mailslot and BLI mailslot designs have more distortion than the podded design.

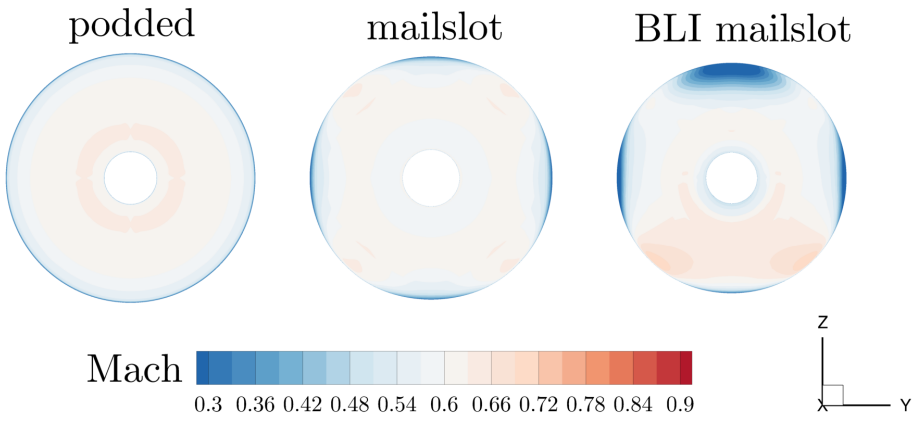


Fig. 18 The fan face Mach distribution of each configuration shows that the mailslot and BLI mailslot designs have more distortion.

The BLI mailslot fan face has a region of slow flow at the very top due to the boundary layer on the wing upstream. Both mailslot designs have faster flow in the corners of the fan face and slower flow along the sides. The slow regions of flow on the left and right are due to the duct increasing in width before the fan face as the rectangular sections converges in area and shape to the circular fan fan. The transition from rectangular to circular sections in the mailslot designs also leads to this faster flow at the corners. The flow is sped up in the corners of the transition sections between the rectangular and circular sections where the curvature from the sides meet. Figure 19 shows streamlines flowing through the edge of the first fan of the optimized mailslot design.

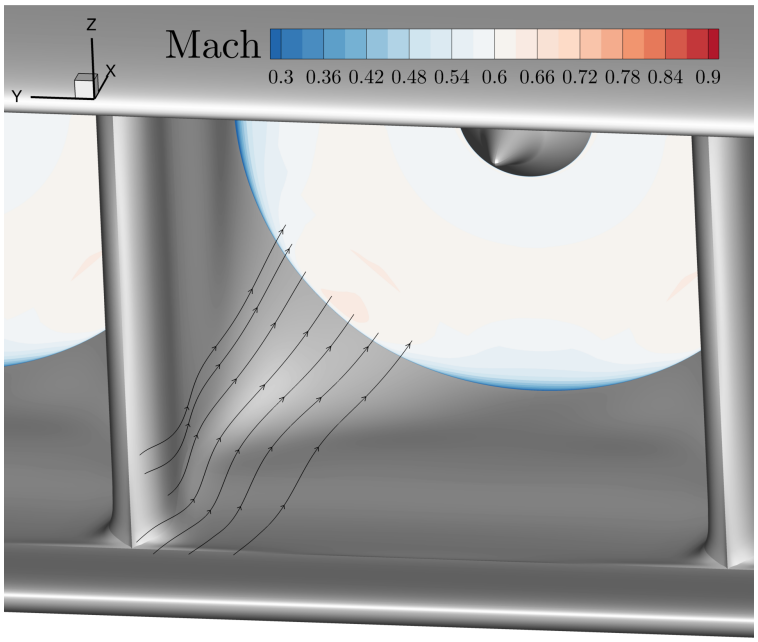


Fig. 19 The transition from rectangular cross-sections to the circular leads to an acceleration at the corner of the transition sections.

VII. Future Work

Despite our best efforts, this work has limitations that invite opportunities for future work. In our optimization study we considered only a single point when evaluating the design, which we did to lower the cost of the optimization. However, using a multipoint approach which considers the performance at a set of design conditions ensures a more robust design. More specifically considering the thrust requirement at the top-of-climb condition and the flow power at the cruise condition would have been more appropriate. Additionally, we did not attempt to account for how the inflow distortion on the fan face would affect the efficiency of the fan or could violate the structural constraints of the fan blades. Future optimization work could improve on this by incorporating a fan face distortion constraint like Gray et al. [23].

We held the number of propulsors in the array constant at 16 to match the design specification of SUSAN. Allowing the optimizer to vary the number of propulsors would be useful earlier in the design cycle to determine the correct trade-off between using more propulsors with lower pressure ratios vs using a few larger propulsors. Using many smaller propulsors would allow the optimizer to place a greater portion of each propulsor in the boundary layer.

Finally, some of the design variables ended up against their optimization bounds. For example, the variables that controlled the length of the hub and the nacelle were both as large as possible for the mailslot design. In this study we needed to bound the growth of these components to aid the optimization by preventing additional mesh warping failures. But future work should consider additional ways to allow the optimizer more geometric freedom.

VIII. Conclusion

We performed gradient-based shape optimization of a mailslot and BLI mailslot propulsor to find geometries that minimized the flow power required. Using OpenMDAO we constructed a model of the performance of the propulsors

based on RANS CFD. The geometry of these propulsors was parameterized with OpenVSP and allowed the optimizer to modify the cross-sectional shapes of the duct and hub as well as the outer model line defining the wing and external nacelle shape. We used symmetry to reduce the computational cost of the CFD analysis and then scaled the outputs of the analysis to approximate the performance of the entire CFD array.

The results of the optimizations show that the flow power of the mailslot and BLI mailslot designs were about 9% and 15% higher respectively when compared to the conventional podded design. The optimized designs have much longer nacelles and hubs when compared with the optimized podded design. The geometric constraints necessary to create a mailslot design are one possible source of this difference. To create the same gradual transition in external height present in the podded design and to smooth out the transition from rectangular to circular sections the inlet and outlet of the mailslot need to be much longer . Furthermore, as a result the increase in viscous drag from stretching the mailslot geometry outweighed the reduction in viscous drag from placing the propulsors in one continuous array with shared surfaces.

Acknowledgments

This work was funded by the Convergent Aeronautics Solutions (CAS) project, which is part of the Transformational Aeronautics Concepts Program (TACP), under the NASA Aeronautics Mission Directorate (ARMD). The authors would also like to acknowledge Leonardo Machado and Timothy Chau for their many helpful discussions on the concepts in this paper. Additional thanks go to Brandon Lowe and Luis Santos Fernandes for reviewing a draft of this paper. Our gratitude also goes to the MDOLab at the University of Michigan for creating and maintaining the open-source computational tools used in this work. Computational resources were supplied by NASA's High-End Computing (HEC) Program via the NASA Advanced Supercomputing (NAS) Division at the Ames Research Center.

References

[1] Brelje, B., and Martins, J. R. R. A., "Electric, Hybrid, and Turboelectric Fixed-Wing Aircraft: A Review of Concepts, Models, and Design Approaches," *Progress in Aerospace Sciences*, Vol. 104, 2019, pp. 1–19. https://doi.org/10.1016/j.paerosci.2018.06.004.

[2] Jansen, R. H., Kiris, C. C., Chau, T., Kenway, G. K., Machado, L. G., Duensing, J. C., Mirhashemi, A., Haglage, J. M., Timothy, P. D., Chapman, J. W., French, B. D., Goodnight, T. W., Miller, L. R., Litt, J. S., Denham, C. L., Lynde, M., Campbell, R., Hiller, B., and Heersema, N., "Subsonic Single Aft Engine (SUSAN) Transport Aircraft Concept and Trade Space Exploration," *AIAA Science and Technology Forum and Exposition, AIAA SciTech Forum 2022*, American Institute of Aeronautics and Astronautics Inc, AIAA, 2022. https://doi.org/10.2514/6.2022-2179.

[3] Machado, L. M., Chau, T., Kenway, G. K., Duensing, J. C., and Kiris, C. C., "Preliminary Assessment of a Distributed Electric Propulsion System for the SUSAN Electrofan," *AIAA SCITECH 2023 Forum*, American Institute of Aeronautics and Astronautics (AIAA), 2023. https://doi.org/10.2514/6.2023-1748.

[4] Wick, A. T., Hooker, J. R., Hardin, C. J., and Zeune, C. H., "Integrated aerodynamic benefits of distributed propulsion," *53rd AIAA Aerospace Sciences Meeting*, American Institute of Aeronautics and Astronautics Inc, AIAA, 2015, pp. 1–36. https://doi.org/10.2514/6.2015-1500.

[5] Schmollgruber, P., Donjat, D., Ridel, M., Cafarelli, I., Atinault, O., François, C., and Paluch, B., "Multidisciplinary Design and performance of the ONERA Hybrid Electric Distributed Propulsion concept (DRAGON)," *AIAA Scitech 2020 Forum*, 2020. https://doi.org/10.2514/6.2020-0501.

[6] Lee, B. J., and Liou, M.-F., "Conceptual Design of Propulsors for the SUSAN Electro-fan Aircraft," *AIAA SCITECH 2022 Forum*, 2022. https://doi.org/10.2514/6.2022-2305.

[7] Machado, L., Chau, T., Kenway, G., Duensing, J. C., and Kiris, C. C., "High-Fidelity Aerodynamic Analysis and Optimization of the SUSAN Electrofan Concept," *AIAA Science and Technology Forum and Exposition, AIAA SciTech Forum 2022*, American Institute of Aeronautics and Astronautics Inc, AIAA, 2022. https://doi.org/10.2514/6.2022-2304.

[8] Machado, L. M., Chau, T., and Duensing, J., "Toward the Development of an Underwing Boundary Layer Ingesting Distributed Propulsion System for the SUSAN Electrofan," *AIAA SCITECH 2024 Forum*, American Institute of Aeronautics and Astronautics (AIAA), 2024. https://doi.org/10.2514/6.2024-1327.

[9] Yildirim, A., Gray, J. S., Mader, C. A., and Martins, J. R. R. A., "Coupled Aeropropulsive Design Optimization of a Podded Electric Propulsor," *AIAA Aviation Forum*, 2021. https://doi.org/10.2514/6.2021-3032.

[10] Lamkin, A. H., Yildirim, A., and Martins, J. R. R. A., "Coupled aeropropulsive analysis and optimization of a high bypass turbofan engine," *33rd Congress of the International Council of the Aeronautical Sciences*, 2022.

[11] Lamkin, A. H. R., Yildirim, A., Martins, J. R. R. A., and Wukie, N. A., "Advancements in Coupled Aeropropulsive Design Optimization for High-Bypass Turbofan Engines," *AIAA Aviation Forum*, San Diego, CA, 2023. https://doi.org/10.2514/6.2023-3591.

[12] Abdul Kaiyoom, M. A. S., Yildirim, A., and Martins, J. R., "Coupled Aeropropulsive Design Optimization of an Over-Wing Nacelle Configuration," American Institute of Aeronautics and Astronautics (AIAA), 2023. https://doi.org/10.2514/6.2023-0327.

[13] Gray, J. S., and Martins, J. R. R. A., "Coupled Aeropropulsive Design Optimization of a Boundary-Layer Ingestion Propulsor," *The Aeronautical Journal*, Vol. 123, No. 1259, 2019, pp. 121–137. https://doi.org/10.1017/aer.2018.120.

[14] Yildirim, A., Gray, J. S., Mader, C. A., and Martins, J. R. R. A., "Boundary Layer Ingestion Benefit for the STARC-ABL Concept," *Journal of Aircraft*, Vol. 59, No. 4, 2022, pp. 896–911. https://doi.org/10.2514/1.C036103.

[15] Lauer, M. G., and Ansell, P. J., "Aerodynamic Shape Optimization of a Transonic, Propulsion-Airframe-Integrated Airfoil System," *AIAA AVIATION 2022 Forum*, American Institute of Aeronautics and Astronautics Inc, AIAA, 2022. https://doi.org/10.2514/6.2022-3662.

[16] McDonald, R. A., "Interactive Reconstruction of 3D Models in the OpenVSP Parametric Geometry Tool," *53rd AIAA Aerospace Sciences Meeting*, American Institute of Aeronautics and Astronautics, 2015. https://doi.org/10.2514/6.2015-1014.

[17] Gray, J. S., Hwang, J. T., Martins, J. R. R. A., Moore, K. T., and Naylor, B. A., "OpenMDAO: An open-source framework for multidisciplinary design, analysis, and optimization," *Structural and Multidisciplinary Optimization*, Vol. 59, No. 4, 2019, pp. 1075–1104. https://doi.org/10.1007/s00158-019-02211-z.

[18] Chau, T., Anibal, J. L., Lowe, B. M., Machado, L., and Duensing, J. C., "High-Fidelity Aeropropulsive Assessment of Distributed Electric Propulsion and Boundary Layer Ingestion for the SUSAN Electrofan," *AIAA SCITECH 2025 Forum*, American Institute of Aeronautics and Astronautics Inc, AIAA, 2025. https://doi.org/10.2514/6.2022-2305.

[19] Mader, C. A., Kenway, G. K. W., Yildirim, A., and Martins, J. R. R. A., "ADflow: An open-source computational fluid dynamics solver for aerodynamic and multidisciplinary optimization," *Journal of Aerospace Information Systems*, Vol. 17, No. 9, 2020, pp. 508–527. https://doi.org/10.2514/1.I010796.

[20] Yildirim, A., Kenway, G. K. W., Mader, C. A., and Martins, J. R. R. A., "A Jacobian-free approximate Newton–Krylov startup strategy for RANS simulations," *Journal of Computational Physics*, Vol. 397, 2019, p. 108741. https://doi.org/10.1016/j.jcp.2019.06.018.

[21] Spalart, P., and Allmaras, S., "A One-Equation Turbulence Model for Aerodynamic Flows," *La Recherche Aerospatiale*, Vol. 1, 1994, pp. 5–21.

[22] Secco, N., Kenway, G. K. W., He, P., Mader, C. A., and Martins, J. R. R. A., "Efficient Mesh Generation and Deformation for Aerodynamic Shape Optimization," *AIAA Journal*, Vol. 59, No. 4, 2021, pp. 1151–1168. https://doi.org/10.2514/1.J059491.

[23] Gray, J. S., Mader, C. A., Kenway, G. K. W., and Martins, J. R. R. A., "Coupled Aeropropulsive Design Optimization of a Three-Dimensional BLI Propulsor Considering Inlet Distortion," *Journal of Aircraft*, Vol. 57, No. 6, 2020, pp. 1014–1025. https://doi.org/10.2514/1.C035845.

[24] Wu, N., Kenway, G., Mader, C. A., Jasa, J., and Martins, J. R. R. A., "pyOptSparse: A Python framework for large-scale constrained nonlinear optimization of sparse systems," *Journal of Open Source Software*, Vol. 5, No. 54, 2020, p. 2564. https://doi.org/10.21105/joss.02564.

[25] Hajdik, H. M., Yildirim, A., Wu, N., Brelje, B. J., Seraj, S., Mangano, M., Anibal, J. L., Jonsson, E., Adler, E. J., Mader, C. A., Kenway, G. K. W., and Martins, J. R. R. A., "pyGeo: A geometry package for multidisciplinary design optimization," *Journal of Open Source Software*, Vol. 8, No. 87, 2023, p. 5319. https://doi.org/10.21105/joss.05319.

[26] Yildirim, A., Jacobson, K. E., Anibal, J. L., Stanford, B. K., Gray, J. S., Mader, C. A., Martins, J. R. R. A., and Kennedy, G. J., "MPhys: A Modular Multiphysics Library for Coupled Simulation and Adjoint Derivative Computation," *Structural and Multidisciplinary Optimization*, 2024. (In press).

[27] Bons, N. P., and Martins, J. R. R. A., "Aerostructural Design Exploration of a Wing in Transonic Flow," *Aerospace*, Vol. 7, No. 8, 2020, p. 118. https://doi.org/10.3390/aerospace7080118.